RSC Advances

PAPER

View Article Online
View Journal | View Issue

Cite this: *RSC Adv.*, 2017, **7**, 33764

Effect of graphene oxide on anticorrosion performance of polyelectrolyte multilayer for 2A12 aluminum alloy substrates

Xia Zhao,*[a] Zuquan Jin,*[b] Binbin Zhang,[a] Xiaofan Zhai,[a] Shuan Liu,[c] Xiaolin Sun,[ab] Qingjun Zhu[a] and Baorong Hou[a]

Received 20th April 2017
Accepted 19th June 2017

DOI: 10.1039/c7ra04458e

rsc.li/rsc-advances

Corrosion of aluminum alloys (Al alloys) has been a ubiquitous problem, and this seriously restricts its range of applications. Herein, a layer-by-layer (LBL) self-assembly method based on the formation and deposition of polyelectrolyte multilayers was employed to fabricate anticorrosion layers on 2A12 Al alloys for corrosion protection. LBL self-assembled films, with and without graphene oxide, were formed on Al alloy surface. The surface morphologies, roughness and chemical compositions of the as-fabricated LBL self-assembled films were characterized by several methods, such as, SEM, AFM, and XPS techniques. The electrochemical properties of the specimens were determined by EIS measurements. The comprehensive equivalent circuits were established to analyze the anticorrosion performance and inhibition efficiency of the resultant LBL self-assembled surfaces. The results indicate that the LBL self-assembled film exhibits inhibition efficiency over 99% in a 3.5% NaCl solution. After dragging to a distance of 200 mm or 400 mm, the inhibition efficiency of the LBL self-assembled film containing graphene oxide can still exceed 96%. LBL self-assembled films are considered to provide a new strategy for marine corrosion protection.

1. Introduction

Corrosion of metallic materials is a ubiquitous problem, which generally costs several percent of its annual gross domestic product (GDP) of an industrialized country. For example, in the USA, the cost of corrosion accounts for 2% to 5% of the national GDP.[1,2] Al alloy is one of the most widely used metallic materials in industrial applications. Over the past decades, Al alloys have drawn much attention of both researchers and engineers as a promising material for aviation, automobiles, electrical appliances and machinery industry due to their light-weight, good castability and anticorrosive qualities.[3–8] They can also be considered as competing materials for cast iron, plastics and even for steels when being applied for operation under conditions of high mechanical loads and moderate sliding speeds (moderate operation temperatures).[9]

In general, a thin and continuous oxide film is naturally formed on the surface of Al alloys, which can prevent the corrosive medium in common atmospheric environment.[10] However, when Al alloys are used in the moist, salt-fog or harsh industrial environments, two most common corrosion types, namely galvanic corrosion and pitting corrosion, appear resulting from the existence of some impurity elements in Al alloys, such as Pb, Sn and Bi.[11–13] As a result of typical corrosion, mechanical properties and durability of the substrates are greatly affected, limiting their further potential applications. Therefore, it is quite necessary to take effective measures to improve the corrosion resistance of alloys in a corrosive environment.[14] Traditionally, the anticorrosion strategies of Al alloys mainly consist of anodic oxidation,[15,16] chemical transformation[17] and organic coating,[18] *etc.* Although the protection efficiency is significantly improved by these methods, the preparation processes are tedious and harmful to the environment. Therefore, it is greatly desirable and challengeable nowadays to develop a simple and environmental friendly method to replace the previous methods due to future environment legislation.

Recently, a layer-by-layer (LBL) self-assembly method has been developed as a promising technique with evident advantages, such as simplicity, versatility and controllability for synthesis of composite functional film, which has attracted great interest of researchers as a strategy for creating anticorrosion films. The functional film is a polyelectrolyte multilayer, which is formed by constructing the polyelectrolyte with positive and negative charges through electrostatic adsorption layer by layer onto the metal surface.[19–21] This approach was first

[a]*Key Laboratory of Marine Environmental Corrosion and Bio-fouling, Institute of Oceanology, Chinese Academy of Sciences, Qingdao 266071, China. E-mail: zx@qdio.ac.cn; zhangbinbin11@mails.ucas.ac.cn; zxf_8968@163.com; brhou@qdio.ac.cn; 1518438510@qq.com; zhuqingjun@qdio.ac.cn; Tel: +86-532-82898731*

[b]*School of Civil Engineering, Qingdao Technological University, Qingdao 266033, China. E-mail: jinzuquan@126.com; Tel: +86-532-85071218*

[c]*Key Laboratory of Marine Materials and Related Ningbo Technologies, Institute of Materials Technologies and Engineering, Chinese Academy of Sciences, Ningbo 315201, China. E-mail: liushuan@nimte.ac.cn; Tel: +86-574-86325713*

proposed by Decher *et al.*[22] in 1992. It proved that at least 100 consecutively alternating layers can be assembled to form the multilayer films on a metal surface.[23] In the following years, the LBL film, prepared by different polyelectrolytes, was widely used for different applications, such as in antibacterial agents,[24] sensors,[25] photocatalysts[26] and anticorrosion agents.[27,28] Graphene oxide (GO) is one of the main precursors of graphene-based materials and is highly promising for various technological applications.[29] It has a two-dimensional spatial structure like graphene, and there are different types of functional groups distributed at the edge and the surface,[30–33] which can provide charges to deposit with other polyelectrolytes to form a LBL film and exhibit better protective ability for materials. Fan *et al.*[34] reported a multilayer polyelectrolyte film prepared by loading GO as an inhibitor on magnesium alloy and investigated its corrosion resistance and self-healing ability, proving that the proposed coating owned a rapid self-healing ability in the presence of water after performing the swelling test on the LBL film-coated samples.

To date, limited studies focused on the performance and anticorrosion mechanism of LBL film loaded with GO on Al alloy surface, and the evaluation of wear resistance of LBL films has not been reported yet. Herein, several issues related to anticorrosion behaviour as well as the mechanism of LBL films were addressed. X-ray photoelectron spectroscopic analysis (XPS), scanning electron microscopy (SEM) and electrochemical impedance spectroscopy (EIS) were employed to analyze the chemical interactions, surface morphologies and corrosion resistance of the fabricated LBL surfaces, respectively. Simultaneously, atomic force microscopy (AFM) was carried out to characterize the roughness of LBL films before and after the wearing test. The principal objective of this study is not only to introduce a new method for modification of Al alloy surface, but also to provide reference resources for potential industrial applications of the protective anticorrosive materials.

2. Experimental

2.1. Materials and reagents

Al alloys (2A12) with a thickness of 3–4 mm were purchased from Beijing Goodwill Metal Technology Co., Ltd. Cerium(iii) nitrate hexahydrate ($Ce(NO_3)_3 \cdot 6H_2O$), acetone, and ethanol were obtained from Sinopharm Chemical Reagent Co., Ltd. Poly(ethyleneimine) (PEI) with a MW of 70 kDa, and GO of 1 wt% were purchased from Shanghai Aladdin Bio-Chem Technology Co, Ltd. Poly(acrylic acid) (PAA) with a MW of 450 kDa was purchased from Sigma-Aldrich. All the reagents were of analytical grade and used without further purification. Deionized water with a resistivity of 18.0 MU cm was used in all the experiments.

2.2. Fabrication of multilayer films

Prior to the test, the surfaces of the specimens were ground with SiC abrasive paper to 800 grit, degreased ultrasonically with acetone, rinsed with distilled water and finally dried in air. Before LBL deposition, the samples were pre-treated with 0.5 M cerium nitrate to form a conversion film because of its combination of remarkable adhesion promotion between metal base and the polymeric top films[35,36] and then dried for 1 h at 80 ± 0.2 °C. The corresponding sample was denoted as Ce-CF. Then, two types of deposition routines were carried out on Ce-CF sample for comparison. The first one was 10 times alternate deposition of 4 mg mL^{-1} PEI and 4 mg mL^{-1} PAA. The second routine was to add 0.2 g L^{-1} GO solution with negative charge as a corrosion inhibitor in the first deposition step. Then, it was deposited by the same method as the first routine with PEI and PAA. After each deposition step, the samples were washed in a mixture of water and ethanol for 5 minutes.

The samples were denoted as LBL-1 and LBL-2 for routine 1 and routine 2, respectively. The principle of our strategy is schematically shown in Fig. 1.

2.3. Characterization

The surface morphologies were recorded using a field-emission scanning electron microscope (FE-SEM) under vacuum at 15 kV (Hitachi S-3400N, Japan). The roughness of the surface was measured using an atomic force microscope (AFM, Multimode 8, Bruker) in tapping mode. The scanning area of AFM measurement was 50 μm × 50 μm, 10 μm × 10 μm and 1 μm × 1 μm. The chemical compositions were measured by XPS (ESCALAB250Xi, Thermo Scientific, Waltham, USA). The spectra were recorded with monochromatized Al Kα radiation (1486.6 eV) as the excitation source with a base pressure of 1.3×10^{-9} mbar, at a constant power of 150 W (15 kV, 10 mA). The pass energy was 20 eV for the high-resolution spectra. The binding energy of adventitious carbon (C 1s: 284.8 eV) was used as a basic reference.

EIS measurements were performed using a Gamry 3000 electrochemical workstation (Gamry Instrument, USA). A classical three-electrode cell system was employed in which a saturated calomel electrode (SCE), a platinum plate and the Al alloy

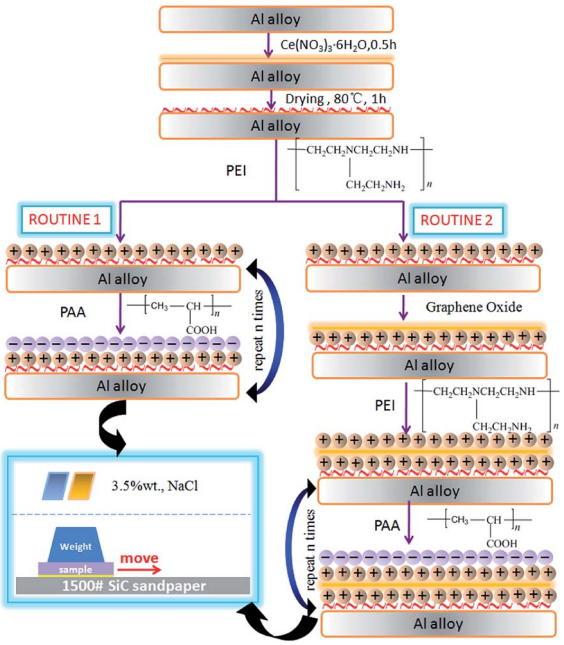

Fig. 1 Schematic of the LBL deposition method.

with or without LBL films were used as the reference electrode, counter electrode and working electrode, respectively. The surface area of the test samples exposed to the corrosion solution was 1 cm^2. EIS measurements were performed over the frequency range from 100 kHz to 10 mHz. A sinusoidal ac perturbation of 20 mV amplitude was applied, and the EIS data collected were analyzed and fitted by electrical equivalent circuit models using the ZSimpWin software.

The wearing test was conducted using a steel block with a weight of 40 g as a pressure, and the pressed area was 20 mm × 20 mm. The gravitational acceleration was a constant of 10 m s^{-2}, and hence the calculated pressure value was about 1.0 kPa. The samples were dragged at a speed of 2 mm s^{-1} to move a distance of 200 mm and 400 mm on 1500 grit SiC sand paper in one direction.

3. Results and discussion

3.1. Surface morphology

The surface topographies and roughness of different films on the Al alloy substrates were characterized by SEM and AFM. Fig. 2 shows the typical SEM images of bare Al alloy and the different resultant films.

The surface of bare Al alloy displayed numerous scratches, as shown in Fig. 2a. After pretreatment with cerium nitrate, a continuous conversion layer with cracks of sizes less than 10 μm was formed on the surface of Al alloy (Fig. 2b). The layer formation mechanism was related to the anodic dissolution of aluminium and cathodic hydrogen evolution:

$$\begin{aligned} &Al \rightarrow Al^{3+} + 3e \\ &Al^{3+} + H_2O + NO_3^- \rightarrow H^+ + AlOHNO_3^+ \\ &2Al + 6H + 4Cl^- \rightarrow 3H_2 + 2AlNO_3^{2+} \\ &2H_2O + O_2 + 4e \rightarrow 4OH^- \end{aligned} \quad (1)$$

The concentration of hydroxyl ions was improved after the electrochemical reaction, which subsequently promoted the deposition of cerium hydroxide and cerium oxide on the surface.[37–39] These cracks facilitated mechanical binding for the following deposition of polymer multilayers.[34] For specimens without graphene oxide, the positively charged PEI and negatively charged PAA were alternatively deposited on the cerium-based conversion layer. With the deposition of polyelectrolyte, an inhomogeneous but non-cracking surface can be observed on the sample of LBL-1 (Fig. 2c). Fig. 2d shows the morphology of LBL-2 specimen and the surface is observed to be denser and darker with some curly fold due to the addition of GO.

Fig. 3 shows the corresponding AFM tapping mode 3D images of LBL-1 and LBL-2 with different scanning areas, illustrating the surface roughness of the LBL self-assembling film. In Fig. 3a, for LBL-1 with a scanning area of 10 × 10 μm^2, the average roughness (R_a) and root-mean-square roughness (R_q) were found to be 48.6 nm and 64.1 nm, respectively, and for that with a scanning area of 1 × 1 μm^2, R_a and R_q values were 7.67 nm and 9.83 nm, respectively. In Fig. 3b, for LBL-2 with a scanning area of 10 × 10 μm^2, R_a and R_q values were found to be 23.4 nm and 31.0 nm, respectively, and for that with a scanning area of 1 × 1 μm^2, R_a and R_q values were 4.88 nm and 6.31 nm, respectively. Compared with Fig. 2, the 3D images of Fig. 3 were more intuitive to show the corresponding morphology of the LBL self-assembling film. There were significant differences in these two self-assembling films. From the perspective of roughness value, R_a and R_q values of LBL-1 were clearly higher than those of LBL-2 whether for the scanning area of 10 × 10 μm^2 or for 1 × 1 μm^2.

From the view of the geometric shape of 1 × 1 μm^2 scanning area, the surface of LBL-1 liked large-scale rolling hills, whereas, for LBL-2, it presented numerous hills with a sharp peak. All the differences suggested that GO had a great impact on the surface state of the film and it was conductive to form the uniform and smooth self-assembling film, which might have finally affected the anticorrosion properties of the self-assembling film.

3.2. Chemical composition of protective films

XPS was utilized to analyze the chemical compositions of different films on Al alloy substrates. Fig. 4a–c reveal the XPS

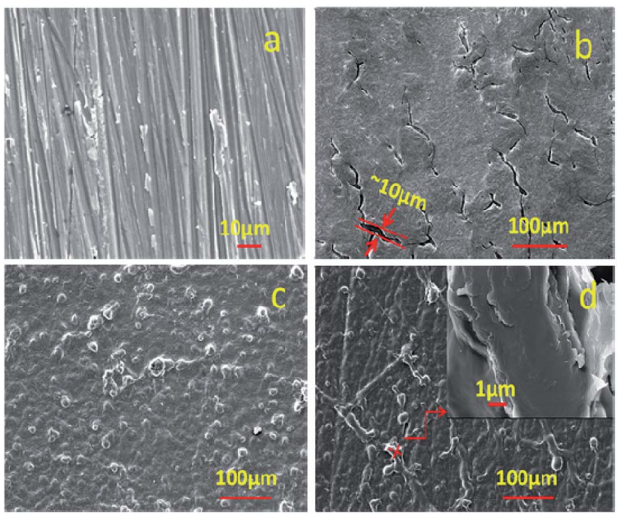

Fig. 2 SEM images of (a) bare Al alloy, (b) Ce-CF, (c) LBL-1 and (d) LBL-2.

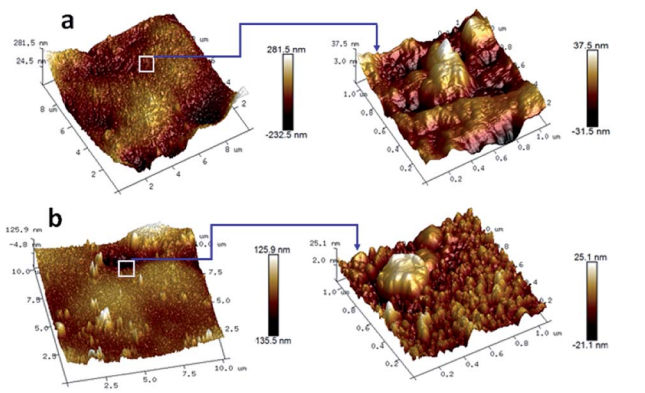

Fig. 3 AFM tapping mode 3D images of (a) LBL-1 and (b) LBL-2 with scanning areas of 10 × 10 μm^2 (left) 1 × 1 μm^2 (right).

survey spectra, Ce 3d and O 1s decomposition fitted curve of XPS spectrum for Ce conversion film, respectively. According to the figures, the presence of Ce and O can be observed.

Typically, the Ce 3d XPS spectrum in Fig. 4b exhibited three lobed envelopes, around 879–890 eV, 895–910 eV and 917 eV, individually. As the heating process promoted the oxidation of cerium, some part of Ce^{3+} was transformed into Ce^{4+}. These envelopes confirmed the coexistence of both Ce^{3+} and Ce^{4+},[40] as well as O 1s spectrum (Fig. 4c); two bonds of Ce with O were formed, which were CeO_2 with a binding energy of 529.0 eV and CeOOH with a binding energy of 531.3 eV. The XPS survey spectrum of the LBL-1 sample mainly showed the presence of C, O, and N on the surface of LBL-1, as shown in Fig. 4d. Fig. 4e and f show the C 1s and N 1s decomposition fitted curves of the XPS spectra for LBL-1 sample, respectively, which were investigated for further confirmation of the chemical composition of the LBL self-assembling film. As a result, the C 1s spectrum of LBL-1 showed two peaks with a bonding energy of 284.6 eV and 286.8 eV, which is due to the bonds of C–H and C═O, respectively, while there were two peaks for N 1s spectrum in Fig. 4f: one located at 399.1 eV, assigned to C–NH–C group, and the other was at 399.8 eV, which corresponded to O═C–NH–C group.

The XPS survey spectrum of the LBL-2 sample mainly showed the presence of C, O, and N on the surface of LBL-2, as shown in Fig. 4g. Fig. 4h and i present the C 1s and N 1s decomposition fitted curves of the XPS spectra for LBL-2 sample, respectively, which were employed for the comparison of chemical composition with that of LBL-1 sample. The C 1s spectrum of LBL-2 displays two peaks with bonding energies 284.3 eV and 285.3 eV, which were attributed to C element and O═C–CH_2 bond, separately. The difference in C 1s spectrum peak type and location was due to GO in LBL-2. The N 1s spectrum in Fig. 4i revealed two peaks at 399.1 eV and 399.8 eV, which was the same as that in Fig. 4f; moreover, the peak areas were larger than that in Fig. 4f. For O═C–NH–C bond at 399.8 eV of LBL-2, the peak area was about 2 times that of LBL-1, signifying that the occupy ratio of O═C–NH–C bond is increased, while the occupy ratio of C–NH–C bond is reduced.

The XPS results indicated that LBL-1 and LBL-2 were successfully deposited onto the specimen surface. As several functional groups were introduced in the production process of GO, such as epoxy, hydroxyl, carboxyl, and carbonyl,[41] the

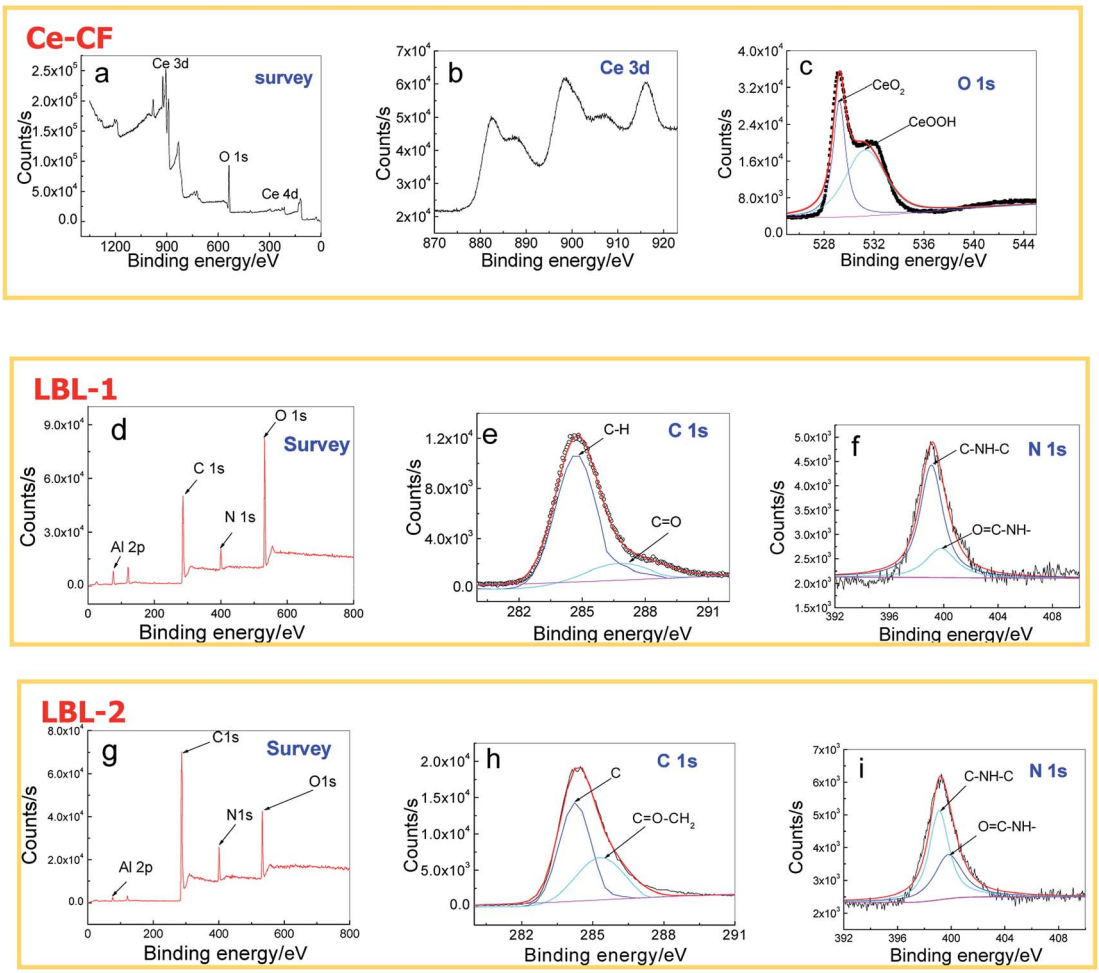

Fig. 4 XPS of different films: (a), (b) and (c) are for Ce-CF; (d), (e) and (f) are for LBL-1; (g), (h) and (i) are for LBL-2. The black lines are the determined results; the red lines are the total fitted curves; the blue and green lines are the decomposition fitted curves.

chemical bonds in LBL-2 sample were different from those of LBL-1 under the influence of these functional groups. A large number of carboxyl groups in grapheme oxide can react with the amino group to form O=C–NH–C bonds with higher bond energy than that of C–NH–C bond, which endow LBL-2 film with more stability than LBL-1 film.[42] The reaction diagram of GO and PEI is illustrated in Fig. 5.

3.3. Electrochemical properties

The anticorrosion performance is a key factor in evaluating the possibilities of the protective film in fundamental research and practical applications.[43] The electrochemical behaviors of the blank Al alloy, Al alloy with Ce-CF, LBL-1 and LBL-2 were determined in 3.5 wt% NaCl solution, individually, and the results are illustrated in Fig. 6.

In Fig. 6a, it can be seen that all curves presented capacitive properties. In addition, for the four samples, the radii of the capacitive arc were different, indicating various protective abilities of these samples; for the blank sample, it was the smallest, followed by Ce-CF, LBL-1 and LBL-2 samples. In Fig. 6b, the total system impedance similarly followed the law of blank sample, Ce-CF, LBL-1 and LBL-2. For phase angle in Fig. 6c, except the blank sample, all the other samples presented multi time-constants features. To quantify the corrosion resistance of different samples, equivalent electrical circuits were established to fit the EIS results, and the detailed discussions are addressed in the next section.

Fig. 7 illustrates the diagram of equivalent circuit models used for fitting the measured EIS data, and the fitted line is presented along with the measured data in points in Fig. 6. For Al alloy, the Nyquist spectrum presented only one capacitive

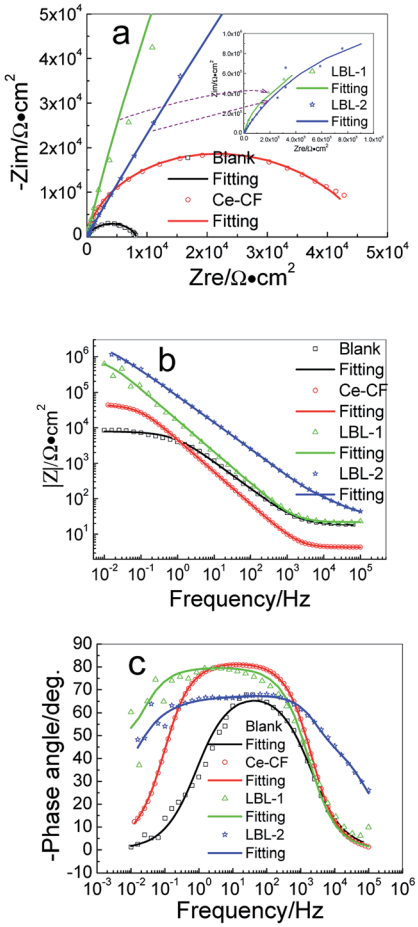

Fig. 6 EIS plots and the fitting curves of Al alloy samples with different film. (a) Nyquist plots; (b and c) Bode plots.

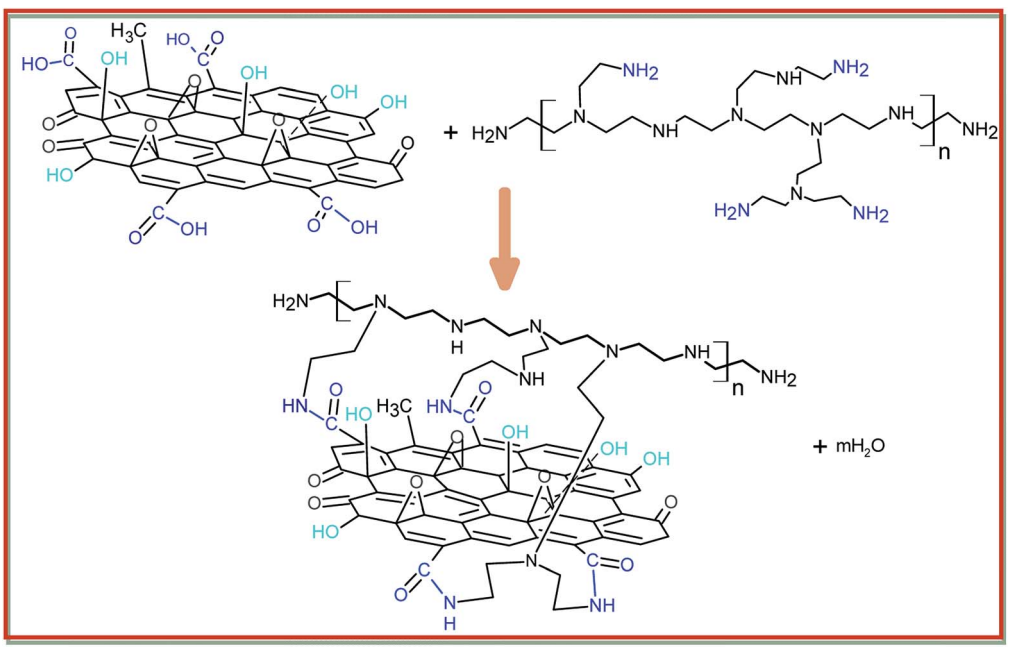

Fig. 5 Reaction diagram of GO and PEI.

semicircle. This can be attributed to the fact that the surface of bare Al alloy was abraded by the SiC sand paper, and there was no film formed on the metal surface. Therefore, the characterization of the determined curve was the charge-transfer process at the solution/alloy interface. Thus, the corrosion parameters were fitted by model 1, and the code should be described as $R_s(Q_{dl}R_{ct})$. R_s denotes the solution resistance, and Q_{dl} and R_{ct} represent the double-layer capacitance and the charge-transfer resistance of the interfacial double electric layer, respectively. Specially, in this study, all the constant phase elements Q were used to model the capacitance because of the heterogeneity of the electrode surface.[44] The impedance of Q is expressed as

$$Z_Q = \frac{1}{Y_0(j\omega)^n} \quad (2)$$

herein, Y_0 and n are the coefficient and the exponent, respectively, ω is the angular frequency in rad s^{-1} ($\omega = 2\pi f$), and j is the imaginary unit with $j^2 = -1$.[45]

For Ce-CF sample, the curve in Fig. 6a showed a depressed capacitive semicircle. Essentially, this semicircle was formed by two overlapping semicircles, a high-frequency one and a low-frequency one, which correspond to two electrochemical processes. The high-frequency semicircle was related to the Ce conversion film, whereas the low-frequency semi-circle corresponded to the charge-transfer process. Because there were numerous defects in the conversion film as shown in Fig. 2b, the corrosive medium could penetrate the conversion film directly through these cracks into the film/metal interface, which resulted in various series connection of these two electrochemical processes, as displayed by model 2. In addition, the total model code can be expressed as $R_s(Q_{con}R_{con})(Q_{dl}R_{ct})$, in particular Q_{con} and R_{con} represent capacitance and resistance of the Ce conversion film, individually.

For LBL-1 sample, 10 layers of polyelectrolytes were deposited on Al alloy with Ce conversion film, the system impedance was close to $10^6\ \Omega\ cm^2$, which was significantly higher than that of the blank sample and Ce-CF sample, suggesting that the layer played a good protection role and the corrosive ions were effectively inhibited from participating in the electrochemical reaction. Thus, it was reasonable to analyze the EIS plots regarding the polyelectrolytes layer as the capacitor. The charges passed through the pores of the polyelectrolyte layers, penetrated into the Ce conversion film, and then arrived at the interface of film/metal. Herein, the state of Ce conversion film was different from the pure Ce conversion film on Al alloy because the polyelectrolytes could fill some inherent cracks of the pure Ce conversion film,[35,36] endowing it with better blocking ability from the corrosive ions. For LBL-2 sample, the system impedance was higher than that of LBL-1 sample because of the function of GO. GO can participate in the absorption process and form a integrated structure with the polyelectrolytes; thus, the electrode process was similar to that of LBL-1 sample. Model 3 was employed to model LBL-1 and LBL-2 samples with three electrode processes on the self-assembling film, Ce conversion film and charge-transfer. The model code can be denoted by $R_s(Q_{LBL}(R_{por}(Q_{con}(R_{con}(Q_{dl}R_{ct})))))$; herein, Q_{LBL} and R_{por} represent the capacitance and the pore solution resistance of the LBL self-assembled film, respectively.

In summary, the total impedance of the three models can be calculated by the following equations:

Model 1:

$$Z_1 = R_s + \frac{1}{\frac{1}{R_{ct}} + Y_{0dl}(j\omega)^{n_3}} \quad (3)$$

Model 2:

$$Z_2 = R_s + \frac{1}{\frac{1}{R_{con}} + Y_{0con}(j\omega)^{n_2}} + \frac{1}{\frac{1}{R_{ct}} + Y_{0dl}(j\omega)^{n_2}} \quad (4)$$

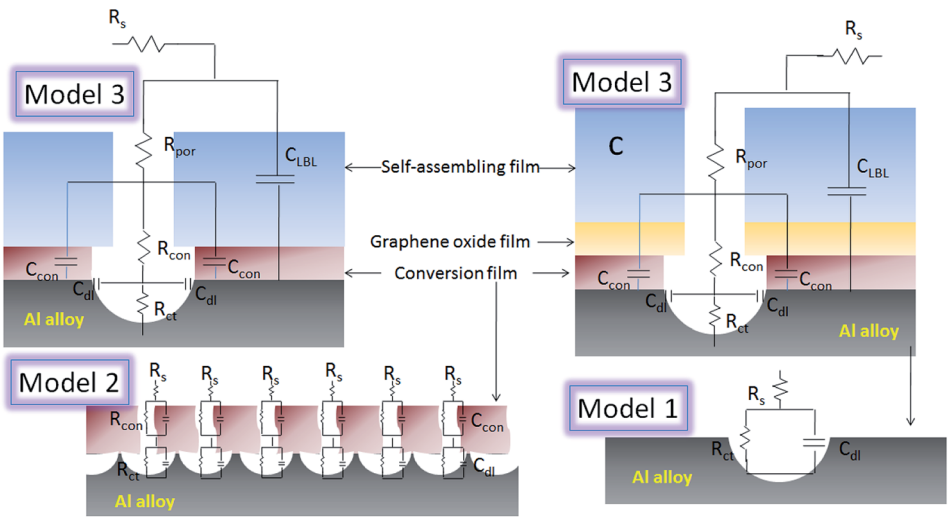

Fig. 7 Equivalent circuits of EIS plots for Al alloy samples with different films.

Model 3:

$$Z_3 = R_s + \cfrac{1}{Y_{0LBL}(j\omega)^{n_1} + \cfrac{1}{R_{por} + \cfrac{1}{Y_{0con}(j\omega)^{n_2} + \cfrac{1}{R_{con} + \cfrac{1}{\cfrac{1}{R_{ct}} + Y_{0dl}(j\omega)^{n_2}}}}}} \quad (5)$$

The electrochemical parameters were obtained from simulation of the EIS data from Fig. 5 and are illustrated in Table 1. The inhibition efficiency (η) is calculated using the following formula:[46]

$$\eta\ (\%) = \left(1 - \frac{R_{ct}^0}{R_{ct}}\right) \times 100\% \quad (6)$$

In Table 1, the R_{ct} value of the blank Al alloy was 8241 Ω cm^2. Once the surface of Al alloy was covered with different films, R_{ct} changed accordingly. The changing law of R_{ct} value followed the order of LBL-2 > LBL-1 > Ce-CF > blank Al alloy. The lowest R_{ct} value of the blank Al alloy indicated that the charge-transfer process occurred more easily compared with the other samples, which was prone to induce corrosion of Al alloy. R_{con} value increased as LBL films were deposited on Ce-CF film compared with the pure Ce-CF film, confirming the fact that the polyelectrolytes can react with the cracked part of Ce conversion film and enhance its protection ability. The higher R_{por} value of LBL-2 sample compared with LBL-1 sample indicated that a more dense film was formed on the Al-alloy surface, which was attributed to GO applied in LBL-2. In GO molecule, there were several carboxyl and hydroxyl groups,[47] which could combine with primary, secondary and tertiary amines in PEI, forming a continuous and high strength film to prevent the corrosive ions effectively. Furthermore, the inhibition efficiency of the protective film to prevent corrosion of the substrate was calculated and it followed the order of LBL-2 > LBL-1 > Ce-CF, providing further evidence for the function of LBL and GO.

As a result, we found that corrosive ions cannot penetrate into the Al alloy substrate to cause corrosion, and the LBL self-assembling film can effectively separate the corrosive medium and protect the underlying substrate, indicating that the self-assembling film can inhibit corrosion of the substrate applied both in marine atmosphere and in natural seawater.

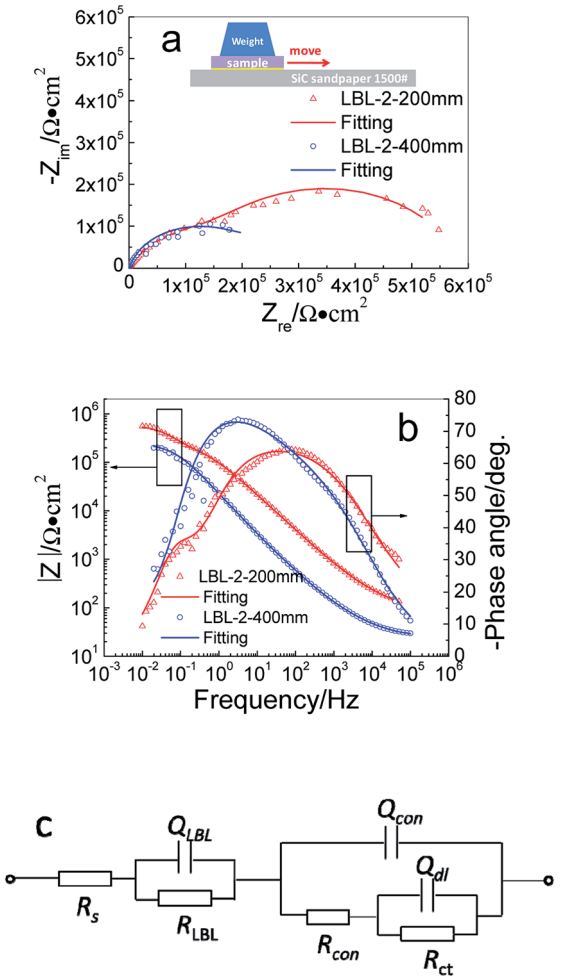

Fig. 8 EIS plots and fitted line for LBL-2 sample after wearing test: (a) Nyquist plots; (b) Bode plots and (c) equivalent circuit.

3.4. Wear resistance

Wear resistance ability is an important parameter for evaluating the anticorrosive durability of the film because film thinning caused by wear is inevitable in the application process of materials. From the EIS analysis and characterization results, it can be concluded that LBL-2 exhibits better protective performance. Based on these results, LBL-2 specimen was taken as the

Table 1 Fitting results of the samples

		Q_{LBL}			Q_{con}			Q_{dl}			
	R_s, Ω cm^2	n_1	Y_{0LBL}, Ω^{-1} cm^{-2} s^n	R_{por}, Ω cm^2	n_2	Y_{0con}, Ω^{-1} cm^{-2} s^n	R_{con}, Ω cm^2	n_3	Y_{0dl}, Ω^{-1} cm^{-2} s^n	R_{ct}, Ω cm^2	η, %
Blank	17.92		—	—	—	—	—	0.78	3.54×10^{-5}	8241	—
Ce-CF	4.334	—	—	—	0.93	1.2×10^{-3}	6081	0.91	4.11×10^{-5}	3.99×10^4	79.3
LBL-1	21.73	0.89	1.19×10^{-5}	7.89×10^5	0.73	4.78×10^{-6}	3.25×10^5	0.90	4.02×10^{-5}	9.98×10^5	99.2
LBL-2	37.73	0.74	3.30×10^{-6}	1.55×10^6	0.92	7.13×10^{-10}	1.32×10^6	0.89	1.88×10^{-5}	3.89×10^6	99.8

Table 2 Fitting results of the LBL-2 sample after being dragged for different distances

		Q_{LBL}			Q_{con}			Q_{dl}			
Dragging distance, mm	R_s, Ω cm^2	n_1	Y_{0LBL}, Ω^{-1} cm^{-2} s^n	R_{LBL}, Ω cm^2	n_2	Y_{0con}, Ω^{-1} cm^{-2} s^n	R_{con}, Ω cm^2	n_3	Y_{0dl}, Ω^{-1} cm^{-2} s^n	R_{ct}, Ω cm^2	η, %
200	22.65	0.22	2.30×10^{-3}	2.33×10^{3}	0.75	2.07×10^{-6}	5.86×10^{4}	0.94	2.58×10^{-6}	5.12×10^{5}	98.4
400	22.22	0.46	2.56×10^{-4}	7.62×10^{2}	0.86	8.76×10^{-6}	1.51×10^{4}	0.82	3.99×10^{-7}	2.15×10^{5}	96.2

sample for dragging test to evaluate the wear resistance performance of the LBL self-assembling film.

Fig. 8 illustrates EIS diagram and the corresponding equivalent circuit of LBL-2 sample dragged on 1500# SiC sandpaper moving for a distance of 200 mm and 400 mm. Moreover, the fitted lines were presented along with the measured data in points in Fig. 8a and b. The dragged sample was denoted as LBL-2-200 mm and LBL-2-400 mm, individually.

The LBL-2 sample was separately dragged to move 200 mm and 400 mm, and two depressed capacitive circles are observed in Fig. 8a, from which it can be seen that the radius of capacitive circles decreased with the increase in dragging distance. The phase angle curves in Fig. 8b indicated that multi time-constants features were present in both samples, considering that more than one peak appeared on the curves. The impedance modulus in Fig. 8b is relatively high, which is up to 10^6 Ω cm^2, suggesting a favorable blocking performance of the samples after the wearing test.

Compared with the initial LBL-2 sample, the system impedance was reduced with the dragging distance, but the value was much higher than that of the blank sample, indicating that the friction specimen still has better blocking properties from the corrosive ions than that of the pure one. In fact, the dragging behavior mainly damaged the surface of the LBL film, it may be thinning by the friction. In this circumstance, the LBL film did not play a dominant role in protecting the substrate metal, which was replaced by the conversion film or the charge-transfer process. Therefore, the LBL film was not hard and perfect enough to be considered as a capacitor. The conversion film was considered to be a capacitor for protecting the substrate. An equivalent circuit including parallel RQ elements connected in series with $Q(R(RQ))$ was proposed for depicting the impedance spectroscopy, as shown in Fig. 8c, and the code can be denoted by $R_s(Q_{LBL}R_{LBL})(Q_{con}(R_{con}(Q_{dl}R_{ct})))$, where, R_{LBL} is the resistance of the LBL film. Correspondingly, the total impedance Z_4 can be calculated using the following equation:

$$Z_4 = R_s + \frac{1}{\frac{1}{R_{LBL}} + Y_{0LBL}(j\omega)^{n_1}} + \frac{1}{Y_{0con}(j\omega)^{n_2} + \frac{1}{R_{con} + \frac{1}{\frac{1}{R_{ct}} + Y_{0dl}(j\omega)^{n_3}}}} \quad (7)$$

Table 2 illustrates the fitting results by equivalent circuit of LBL-2 samples after the wearing test. In Table 2, the R_{LBL} value is smaller than the R_{por} value of LBL-2 in Table 1, indicating that the protection performance of LBL-2 was reduced by the friction behavior. Similarly, the R_{con} and R_{ct} values declined in varying degrees, directly revealing the damage effect caused by the dragging test. With the increase in dragging distance, the resistance values were all reduced, indicated that the longer the dragging distance, the weaker the protective ability the film has.

However, compared with the blank sample, the inhibition efficiency of the abraded sample is still up to 98.4% and 96.2%, indicating that the LBL-2 self-assembled film can still effectively protect the underlying substrate from aggressive media and inhibit electrochemical reaction of the substrate in both marine atmosphere and natural seawater.

In order to further characterize the wear degree of the LBL-2 film surface, AFM was applied to obtain the surface topography of the dragged samples, as shown in Fig. 9.

Fig. 9 shows the corresponding AFM tapping mode 3D images of LBL-2 with a scanning area of 50 × 50 μm^2, illustrating the surface roughness of LBL-2 film before and after the wearing test. In Fig. 9a, before dragging, the R_a and R_q of LBL-2 were found to be 318 nm and 254 nm, respectively. For LBL-2-200 mm in Fig. 9b, the R_a and R_q values were 466 nm and

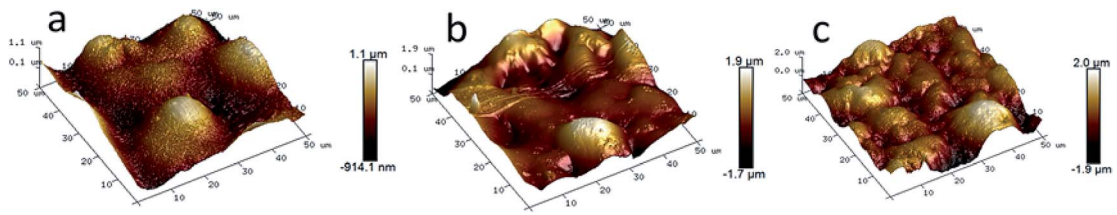

Fig. 9 AFM tapping mode 3D images of LBL-2 before and after wearing with a scanning area of 50 × 50 μm^2: (a) no wear; (b) worn distance = 200 mm and (c) worn distance = 400 mm.

356 nm, respectively, whereas for LBL-2-400 mm in Fig. 9c, the R_a and R_q values were presented to be 520 nm and 403 nm, respectively. Clearly, the surface roughness was increasing with the dragged distance, suggesting a certain extent of wear and damage of LBL-2 film. However, for the geometric shape and the color, the surface of LBL-2 without wear liked a few yurts scattered on the metal with dark color, while after being dragged to move 200 mm, the dome of the initial yurt presented irregular and bright. After dragging to a distance of 400 mm, the number of yurts significantly increased and the size became smaller than the initial size of the yurts at the same site. Thus, it can be concluded that the wearing test had a certain impact on LBL-2 film. The longer the dragging distance of the film was, the higher the average roughness of the film surface would be. The wearing behavior can make the film thinner and thinner, resulting in reduction of the protective function, suggesting that the wear resistance performance should be further improved in the future research.

4. Conclusions

In summary, two types of LBL self-assembling films were successfully produced on Al-alloy surface as an effective blocking layer against corrosive medium, providing a reference strategy for the corrosion protection of metallic substrates. The tentative conclusions are depicted as follows:

(1) LBL self-assembling is a simple and easy operational method providing a valid strategy in designing a protective film against corrosion on Al-alloy surface.

(2) The obtained LBL self-assembling films exhibit greatly enhanced corrosion resistance in 3.5% NaCl solution. The inhibition efficiency of graphene oxide-modified LBL film was approximately 99.8%.

(3) LBL self-assembled film modified by GO has certain wear resistance with the corrosion inhibitive efficiency higher than 96% after dragging to move a distance of 400 mm.

(4) The wear resistance of LBL self-assembling film was expected to be improved in future research studies. In addition, the film was designed to be studied in more potential practical applications, such as anti-contamination, antifouling and anticorrosion in harsh marine environments.

(5) For comprehensive understanding, some other aspects should be researched in the future, such as the concentration of the polyelectrolyte solution, the effect of different numbers of polyelectrolyte layers, different materials like GO and the deep effective mechanism of GO on the wear resistance.

Acknowledgements

This research was supported by the Chinese National Natural Science Foundation (NSF) Grant (No. 5142010501), the China Postdoctoral Science Foundation (No. 2015M580528, 2016T90553) and the Open Project of Key Laboratory of Marine New Materials of CNITECH (LMMT-KFKT-2014-008). The authors gratefully appreciate the financial support provided by the NSF and other Foundations.

References

1 H. H. Uhlig, The cost of corrosion to the United States, *Corrosion*, 1950, **6**, 29–33.
2 M. V. Biezma and J. R. San Cristobal, Methodology to study cost of corrosion, *Corros. Eng., Sci. Technol.*, 2005, **40**, 344–352.
3 T. Savaskan and S. Murphy, Comparative wear behavior of Zn–Al based alloys in an automotive engine application, *Wear*, 1984, **98**, 151–161.
4 H. Jian, Z. Yin, F. Jiang, X. Li and T. Nonferr, EBSD analysis of fatigue crack growth of 2124 aluminum alloy for aviation, *Rare Met. Mater. Eng.*, 2014, **43**, 1332–1336.
5 A. D. Kotov, A. V. Mikhaylovskaya, M. S. Kishchik, A. A. Tsarkov, S. A. Aksenov and V. K. Portnoy, Near net shape casting process for producing high strength 6xxx aluminum alloy automobile suspension parts, *J. Alloys Compd.*, 2016, **688**, 336–344.
6 A. Rac, M. Babić, R. Ninković and J. Balk, Theory and practice of Zn–Al sliding bearings, *J. Balk. Tribol. Assoc.*, 2001, **7**, 234–240.
7 M. Babic and R. Ninkovic, Zn–Al alloys as tribomaterials, *Tribol. ind.*, 2004, **26**, 3–7.
8 M. Babic, R. Ninkovic and A. Rac, Sliding wear behavior of Zn–Al alloys in conditions of boundary lubrication. The Annals of University "Dunărea De Jos" of Galaţi Fascicle VIII, *Tribology*, 2005, 60–64.
9 P. Choudhury, S. Das and B. K. Datta, Effect of Ni on the wear behavior of a zinc–aluminum alloy, *J. Mater. Sci.*, 2002, **37**, 2103–2107.
10 R. Vera, D. Delgado and B. M. Rosales, Effect of atmospheric pollutants on the corrosion of high power electrical conductors: Part 1. Aluminium and AA6201 alloy, *Corros. Sci.*, 2006, **48**, 2882–2900.
11 F. Gharavi, K. A. Matori, R. Yunus, N. K. Othman and F. Fadaeifard, Corrosion evaluation of friction stir welded lap joints of AA6061-T6 aluminum alloy, *Trans. Nonferrous Met. Soc. China*, 2016, **26**, 684–696.
12 C. V. Rao, G. M. Reddy and K. S. Rao, Microstructure and pitting corrosion resistance of AA2219 Al–Cu alloy friction stir welds -Effect of tool profile, *Def. Technol.*, 2015, **11**, 123–131.
13 H. Li, P. Zhao, Z. Wang, Q. Mao, B. Fang, R. Song and Z. Zheng, The intergranular corrosion susceptibility of a heavily overaged Al–Mg–Si–Cu alloy, *Corros. Sci.*, 2016, **107**, 113–122.
14 J. Ou, W. Hu, M. Xue, F. Wang and W. Li, Superhydrophobic surfaces on light alloy substrates fabricated by a versatile process and their corrosion protection, *ACS Appl. Mater. Interfaces*, 2013, **5**, 3101–3107.
15 F. Caubert, P. L. Taberna and L. Arurault, Innovating pulsed electrophoretic deposition of boehmite nanoparticles dispersed in an aqueous solution, into a model porousanodic film, prepared on aluminium alloy 1050, *Surf. Coat. Technol.*, 2016, **302**, 293–301.

16 T. Hashimoto, X. Zhou, P. Skeldon and G. E. Thompson, Structure of the copper–enriched layer introduced by anodic oxidation of copper-containing aluminium alloy, *Electrochim. Acta*, 2015, **179**, 394–401.

17 C. S. Tsao, E. W. Huang, M. H. Wen, T. Y. Kuo, S. L. Jeng, U. S. Jeng and Y. S. Sun, Phase transformation and precipitation of an Al–Cu alloy during non-isothermal heating studied by *in situ* small-angle and wide-angle scattering, *J. Alloys Compd.*, 2013, **579**, 138–146.

18 M. Poorteman, A. Renaud, J. Escobar, L. Dumas, L. Bonnaud, P. Dubois and M. G. Olivier, Thermal curing of *para*-phenylenediamine benzoxazine for barrier coating applications on 1050 aluminum alloys, *Prog. Org. Coat.*, 2016, **97**, 99–109.

19 H. Shi, F. Liu and E. H. Han, Layer-by-Layer polyelectrolyte/inhibitor nanostructures for metal corrosion protection, *J. Mater. Sci. Technol.*, 2015, **31**, 512–516.

20 E. V. Skorb and D. V. Andreeva, Layer-by-Layer approaches for formation of smart self-healing materials, *Polym. Chem.*, 2013, **4**, 4834–4845.

21 J. Carneiro, A. F. Caetano, A. Kuznetsova, F. Maia, A. N. Salak, J. Tedim, N. Scharnagl, M. L. Zheludkevich and M. G. S. Ferreira, Polyelectrolyte-modified layered double hydroxide nanocontainers as vehicles for combined inhibitors, *RSC Adv.*, 2015, **5**, 39916–39929.

22 G. Decher and J. D. Hong, Buildup of ultrathin multilayer films by a self-assembly process, 1. Consecutive adsorption of anionic and cationic bipolar amphiphiles on charged surfaces, in *European conference on organized organic thin films*, 1992, p. 321.

23 G. Decher, J. D. Hong and J. Schmitt, Buildup of ultrathin multilayer films by a self-assembly process: III. Consecutively alternating adsorption of anionic and cationic polyelectrolytes on charged surface, *Thin Solid Films*, 1992, **210–211**, 831–835.

24 Y. Wei, H. C. Hung, F. Sun, T. Bai, P. Zhang, A. K. Nowinski and S. Jiang, Achieving low-fouling surfaces with oppositely charged polysaccharides *via* LBL assembly, *Acta Biomater.*, 2016, **40**, 16–22.

25 S. Pourbeyram, Electrocatalytic determination of H_2O_2 on the electrode modified by LBL assembly of polyoxometalates *via* zirconium ion glue, *Sens. Actuators, B*, 2014, **192**, 105–110.

26 B. J. Starr, V. V. Tarabara, M. Herrera-Robledo, M. Zhou, S. Roualdès and A. Ayral, Coating porous membranes with a photocatalyst: Comparison of LbL self-assembly and plasma-enhanced CVD techniques, *J. Membr. Sci.*, 2016, **514**, 340–349.

27 R. Zeng, L. Liu, K. Luo, L. Shen, F. Zhang, S. Li and Y. Zou, *In vitro* corrosion and antibacterial properties of layer-by-layer assembled GS/PSS coating on AZ31 magnesium alloys, *Trans. Nonferrous Met. Soc. China*, 2015, **25**, 4028–4039.

28 D. V. Andreeva, E. V. Skorb and D. G. Shchukin, Layer-by-Layer Polyelectrolyte/Inhibitor Nanostructures for Metal Corrosion Protection, *ACS Appl. Mater. Interfaces*, 2010, **2**, 1954–1962.

29 S. Qin and Q. Xu, Room temperature ferromagnetism in N_2 plasma treatedgrapheneoxide, *J. Alloys Compd.*, 2017, **692**, 332–338.

30 K. A. Mkhoyan, A. W. Contryman, J. Silcox, D. A. Stewart, G. Eda, C. Mattevi, S. Miller and M. Chhowalla, Atomic and electronic structure of graphene-oxide, *Nano Lett.*, 2009, **9**, 1058–1063.

31 D. R. Dreyer, S. Park, C. W. Bielawski and R. S. Ruoff, The chemistry of graphene oxide, *Chem. Soc. Rev.*, 2010, **39**, 228–240.

32 W. Gao, L. B. Alemany, L. J. Ci and P. M. Ajayan, New insights into the structure and reduction of graphite oxide, *Nat. Chem.*, 2009, **1**, 403–408.

33 D. Li, M. B. Muller, S. Gilje, R. B. Kaner and G. G. Wallace, Processable aqueous dispersions of graphene nanosheets, *Nat. Nanotechnol.*, 2008, **3**, 101–105.

34 F. Fan, C. Zhou, X. Wang and J. Szpunar, Layer-by-layer assembly of a self-healing anticorrosion coating on magnesium alloys, *ACS Appl. Mater. Interfaces*, 2015, **7**, 27271–27278.

35 F. H. Scholes, C. Soste, A. E. Hughes, S. G. Hardin and P. R. Curtis, The role of hydrogen peroxide in the deposition of cerium-based conversion coatings, *Appl. Surf. Sci.*, 2006, **253**, 1770–1780.

36 A. D. Nicolò, L. Paussa, A. Gobessi, A. Lanzutti, C. Cepek, F. Andreatta and L. Fedrizzi, Cerium conversion coating and sol-gel multilayer system for corrosion protection of AA6060, *Surf. Coat. Technol.*, 2016, **287**, 33–43.

37 B. Valdez, S. Kiyota, M. Stoytcheva, R. Zlatev and J. M. Bastidas, Cerium-based conversion coatings to improve the corrosion resistance of aluminum alloy 6061-T6, *Corros. Sci.*, 2014, **87**, 141–149.

38 A. Conde, M. A. Arenas, A. Frutos and J. Damborenea, Effective corrosion protection of 8090 alloy by cerium conversion coatings, *Electrochim. Acta*, 2008, **53**, 7760–7768.

39 A. Frutos, M. A. Arenas, Y. Liu, P. Skeldon, G. E. Thompson, J. Damborenea and A. Conde, Influence of pre-treatments in cerium conversion treatment of AA2024-T3 and 7075-T6 alloys, *Surf. Coat. Technol.*, 2008, **202**, 3797–3807.

40 E. Sheerin, G. K. Reddy and P. Smirniotis, Evaluation of Rh/$Ce_xTi_{1-x}O_2$ catalysts for synthesis of oxygenates from syngas using XPS and TPR techniques, *Catal. Today*, 2016, **263**, 75–83.

41 M. Jin, N. Jiao, C. X. Zhang, H. P. Xiao, K. W. Zhang and L. Z. Sun, Reduction mechanism hydroxyl group from graphene oxide with and without $-NH_2$ agent, *Phys. B*, 2015, **477**, 70–74.

42 J. Conradie and E. Erasmus, XPS Fe 2p peaks from iron tris(*b*-diketonates): Electronic effect of the *b*-diketonato ligand, *Polyhedron*, 2016, **119**, 142–150.

43 B. Zhang, X. Zhao, Y. Li and B. Hou, Fabrication of durable anticorrosion superhydrophobic surfaces on aluminum substrates *via* a facile one-step electrode position approach, *RSC Adv.*, 2016, **6**, 35455–35465.

44 X. Zhao, S. Liu, X. Wang and B. Hou, Surface modification of ZrO_2 nanoparticles with styrene coupling agent and its effect

on the corrosion behaviour of epoxy coating, *Chin. J. Oceanol. Limnol.*, 2014, **32**, 1163–1171.

45 P. Wang, D. Zhang, R. Qiu and J. Wu, Super-hydrophobic metal-complex film fabricated electrochemically on copper as a barrier to corrosive medium, *Corros. Sci.*, 2014, **83**, 317–326.

46 B. Zhang, J. Li, X. Zhao, X. Hu, L. Yang, N. Wang, Y. Li and B. Hou, Biomimetic one step fabrication of manganese stearate superhydrophobic surface as an efficient barrier against marine corrosion and Chlorella vulgaris-induced biofouling, *Chem. Eng. J.*, 2016, **306**, 441–451.

47 C. G. K. Yue, M. N. Ging and H. A. H. Cheng, Identification of functional groups and determination of carboxyl formation temperature in graphene oxide using the XPS O 1s spectrum, *Thin Solid Films*, 2015, **590**, 40–48.